Steady and Dynamic Performance Analysis of a Single-sided Linear Induction Motor

Wei Xu, Jianguo Zhu, Youguang Guo,
Yongchang Zhang, Yi Wang
Faculty of Engineering and Information Technology
University of Technology, Sydney
Sydney, Australia
wxu@eng.uts.edu.au, joe@eng.uts.edu.au

Zhanghai Shi
Department of Electrical Engineering
Hong Kong Polytechnic University
Hong Kong, China
ee.zhhshi@polyu.edu.hk

***Abstract*—The train propelled by a single-sided linear induction motor (SLIM) has been paid much attention recently by both academia and industry. The SLIM drive has advantages such as the direct thrust without the need of friction between wheel and railway track, small cross-sectional area, lack of gear box, and flexible line choice thanks to the greater climbing capability and smaller turning circle compared with a rotary machine drive. However, the SLIM has longitudinal end effect and half-filled slots for its cut-open primary magnetic circuit, which could reduce the air gap average flux linkage and thrust. This paper, based on winding function method, supposes that the SLIM has three groups of windings: primary, secondary fundamental, and secondary end effect windings. The proposed method can consider the actual winding distribution and structure information, and can calculate the mutual-, self-, and leakage inductances for describing the influence of longitudinal end effect and half-filled slots. Then, a new equivalent model is presented to analyze different dynamic and steady state performances. The comprehensive comparison between simulations and experiments indicates that the proposed model can be applied for the SLIM performance prediction and control scheme evaluation.**

Keywords—single-sided linear induction machine (SLIM); longitudinal end effect; winding function method; half-filled slots; equivalent circuit model; steady state performanc; dynamic state performance; linear metro.

I. INTRODUCTION

In recent years, there have been more than 20 urban transportation lines propelled by single-sided linear induction motors (SLIMs) among the world, such as the Kennedy air line in America, linear metro in Japan, Vancouver light train in Canada, Guangzhou subway line 4 in China, and so on. The typical SLIM structure and drive system diagrams are shown in Fig. 1. The primary, similar to the stator of a rotary induction machine (RIM), is hanged below the redirector, which is supplied by the inverter on the vehicle. The secondary, corresponding to the rotor of RIM, is flatted on the railway track, which usually consists of a 5 mm thick copper/aluminum conductance sheet and a 20 mm thick back iron. When the primary three-phase windings are input with AC current, they can build up air flux linkage, which induces eddy current in the secondary sheet. This eddy current will react with aforementioned air gap flux linkage so as to produce a horizontal electromagnetic thrust that can drive the vehicle forward directly without relying on the friction between wheel and track.

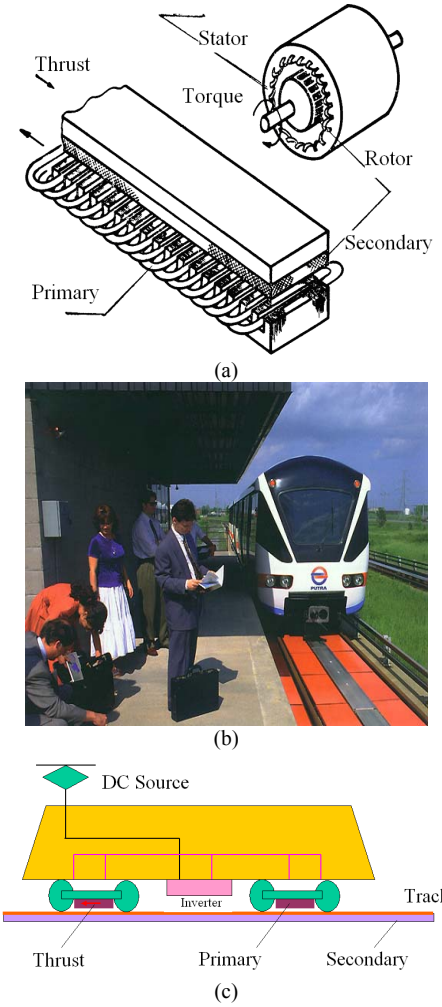

Figure 1. Simple vehicle system diagrams propelled by the SLIM: (a) SLIM structure, (b) photo of urban train, and (c) drive system.

The SLIM drive system has the following merits compared with the RIM drive [1]-[5]. Firstly, it can achieve direct propulsive thrust, which is not dependent on the friction between wheel and rail. Secondly, it has smaller turning radius, smaller cross-sectional area for requirement of a tunnel, larger acceleration, and stronger climbing ability. By investigations from some Japanese exporters, the typical SLIM system has 40-60 m turning radius, 22 m^2 cross-sectional tunnel area, 1.2 m/s^2 acceleration, and 6-8% gradient ability compared with the 80-120 m turning radius, 41 m^2 cross-sectional tunnel area, 0.8 m/s^2 acceleration, and 3-4% gradient ability in a typical

RIM system. Thirdly, it has lower noise and less maintenance. Hence, the SLIM drive system is very suitable to the transportation in large cities.

However, the SLIM, which can be considered as evolved from the RIM, has a cut-open primary magnetic circuit. As the primary moves, a new flux is continuously developed at the primary entrance side, while the air gap flux disappears quickly at the exit side. By the influence of sudden generation and disappearance of the air gap penetrating flux density, an amount of eddy current in anti-direction to the primary current will be induced in the secondary sheet, which correspondingly affects the air gap flux profile along the longitudinal direction (x-axis) as illustrated in Fig. 2. This phenomenon is called "longitudinal end effect" of SLIM, which can increase the copper loss, and decrease the mutual inductance as the velocity goes up. In the end, the effective electromagnetic thrust will be reduced because of the attenuating air gap average flux linkage [5].

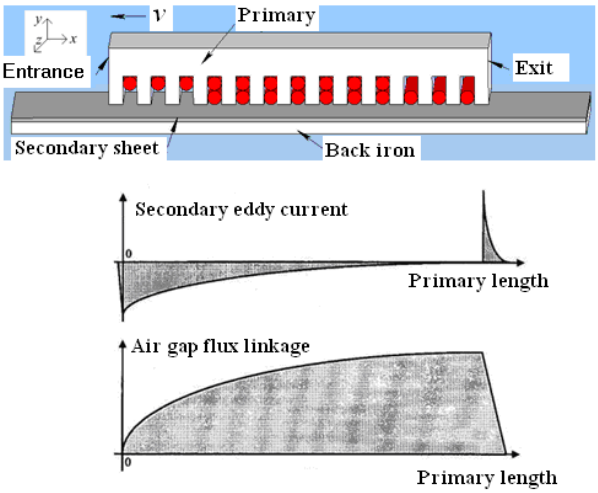

Figure 2. Profiles of secondary eddy current and air gap flux linkage.

Thanks to many researchers' work, plenty of papers have been available on the SLIM longitudinal end effect analysis. Ref. [1] proposed a single phase T-model equivalent circuit to study the SLIM performance. Based on the one dimensional numerical analysis and experimental verification, two coefficients are derived to describe the influence of the longitudinal end effect on the mutual inductance and secondary equivalent resistance. This method can be adopted in a wide speed region and with different air gap widths. However, it is not suitable for studying the SLIM dynamic performance or vector control scheme for it is only a steady state equivalent circuit. Refs. [2] and [3] presented one simple, useful function according to the secondary eddy current average value and energy conversion balance theorem. The function is affected by the SLIM speed, secondary resistance, secondary inductance, and some structural parameters, such as the primary length, which can be employed easily in vector control schemes. However, the function derivation process is very coarse that brings an increasing error as the velocity goes up. Ref. [4] can theoretically simulate steady-state and dynamic performance by using space harmonic method, and the calculation result has comparatively high accuracy. However, it requires substantially more computing time to gain some useful data, which accuracy depends closely on many initially given parameters. If some key values are not initialized rationally, the final solution cannot be obtained due to non-convergence.

This paper, based on the winding function method, presents a new model for conveniently analyzing both the steady and dynamic performances of SLIM. By the primary winding distribution, the longitudinal end effect and half-filled slots located in the primary ends are taken into consideration.

II. Equivalent Circuit Equation of the SLIM

From Ampere's law, Faraday's law and Maxwell's law, the air-gap flux density equation of SLIM can be expressed by [5]

$$\frac{\partial^2 b_y}{\partial x^2} - \sigma\mu_0 v_2 \frac{\partial b_y}{\partial x} - j\sigma\mu_0\omega_e b_y = -j\mu_0 \frac{\pi}{\tau} J_1 e^{j(\omega_e t - \pi x/\tau)} \tag{1}$$

where σ is the secondary conductivity, μ_0 the air permeability, v_2 the primary operating speed, ω_e the angular speed of primary power supply, τ the primary pole pitch, J_1 the equivalent primary sheet current density, and b_y the flux density in the y-axis direction. The solution of $b_y(x, t)$ is

$$b_y(x,t) = \dot{B}_0 e^{-j\frac{\pi x}{\tau}} + \dot{B}_1 e^{-\frac{x}{\alpha_1}} e^{-j\frac{\pi x}{\tau_e}} + \dot{B}_2 e^{\frac{x}{\alpha_2}} e^{j\frac{\pi x}{\tau_e}} \tag{2}$$

where b_y consists of three parts, B_0, B_1 and B_2. B_0 is the normal traveling wave which travels forward like the fundamental flux density in the RIM. B_1 and B_2, determined from boundary conditions, are the entrance and exit end-effect waves, respectively. α_1 is the penetration depth of entry-end-effect wave, α_2 the penetration depth of exit-end-effect wave, and τ_e the half wavelength of end effect wave, which are functions of speed and motor structural parameters [5].

On the base of air-gap flux density equation, this paper divides SLIM secondary winding function into fundamental and end effect component. Firstly it deduces the primary two-phase stationary axis model according to the primary winding distribution. Then, the secondary fundamental and end effect parts are gained separately from the steady state and dynamic state of air gap magnetic flux equations. Moreover, it calculates all inductances, goodness factor, secondary resistance and speed voltage coefficients. On the energy conversion relationship between primary and secondary, the mathematic expressions of thrust, power factor and efficiency are derived. Generally, the whole derivation progress is complex, and more details can be found in [5]. A brief summary is made below.

The primary stationary three-axis winding functions are

$$\begin{cases} N_{as}(x) = \dfrac{N_s}{2}\cos(\pi x/\tau + \pi) \\ N_{bs}(x) = \dfrac{N_s}{2}\cos(\pi x/\tau + \pi/3) \\ N_{cs}(x) = \dfrac{N_s}{2}\cos(\pi x/\tau - \pi/3) \end{cases} \tag{3}$$

where N_s is the fundamental part per pole winding series.

In order to gain the stationary two-axis stator winding function expressions, $N_{\alpha s}$ and $N_{\beta s}$, from the stationary three-axis winding distributions, the following rules according to the flux linkage balance theory should be obeyed by

$$N_{as}(x)i_{as}+N_{bs}(x)i_{bs}+N_{cs}(x)i_{cs}=N_{\alpha s}(x)i_{\alpha s}+N_{\beta s}(x)i_{\beta s} \quad (4)$$

where $i_{\alpha s}$ and $i_{\beta s}$ can be achieved from i_{as} , i_{bs} and i_{cs} by using static 3/2 coordination transformation. Hence, the primary stationary two-axis winding functions are expressed by

$$\begin{cases} N_{\alpha s}(x)=\dfrac{3}{4}N_s\sin(\pi x/\tau) \\ N_{\beta s}(x)=-\dfrac{3}{4}N_s\cos(\pi x/\tau) \end{cases} \quad (5)$$

The secondary winding functions including both the fundamental and end effect parts are abstract, which can be gained from the electromagnetic relationship between primary and secondary [3] [4]. The secondary fundamental winding function $\dot{N}_{rs}$ is derived by

$$\dot{B}_{rs}=\frac{\mu_0}{g_e}\dot{N}_{rs}\dot{I}_{rs} \quad (6)$$

where $\dot{B}_{rs}$, $\dot{I}_{rs}$ and g_e are the secondary fundamental complex flux density, secondary fundamental complex current and equivalent electromagnetic air gap width respectively. From the air gap flux density steady equation, $\dot{B}_{rs}$ can be expressed by

$$\dot{B}_{rs}=\frac{(3\mu_0/4g_e)N_s}{\sqrt{1+(1/sG)^2}}I_s\exp[j(\omega_e t-\pi x/\tau+\theta_s)] \quad (7)$$

where s is the slip, G the goodness factor, θ_s the angle between the primary and secondary fundamental currents, and I_s the RMS value of primary phase current. From the T-model equivalent circuit of one dimension, $\dot{I}_{rs}$ can be drawn by

$$\dot{I}_{rs}=\dot{I}_s\frac{-jX_m}{jX_m+\dfrac{R_r}{s}}=\frac{-I_s}{\sqrt{1+(1/sG)^2}}\exp[j(\omega_e t+\theta_s)] \quad (8)$$

where X_m and R_r are the mutual inductance and secondary resistance. Hence, from (6) to (8), the secondary fundamental winding functions $\dot{N}_{rs}$ are indicated by

$$\begin{cases} N_{\alpha rs}(x)=\dfrac{3}{4}N_s\sin(\pi x/\tau) \\ N_{\beta rs}(x)=-\dfrac{3}{4}N_s\cos(\pi x/\tau) \end{cases} \quad (9)$$

Similar with the solution of secondary fundamental part, the secondary end effect part winding function $\dot{N}_{re}$ can be deduced by

$$\dot{B}_{re}=\frac{\mu_0}{g_e}\dot{N}_{re}\dot{I}_{re} \quad (10)$$

where $\dot{B}_{re}$ and $\dot{I}_{re}$ are the secondary end effect complex flux density and secondary end effect complex current, respectively. From the air gap flux density dynamic equation, $\dot{B}_{re}$ can be derived by

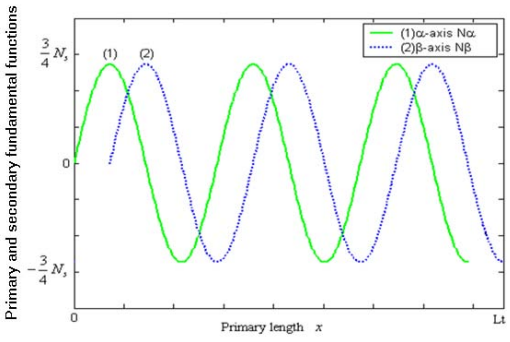

(a)

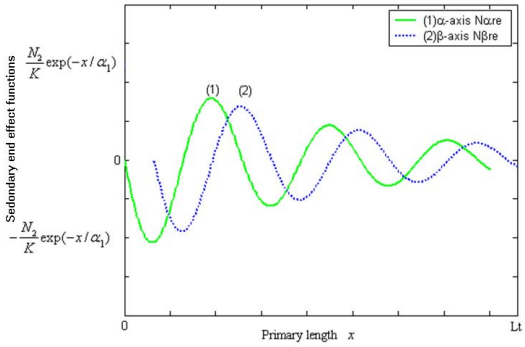

(b)

Figure 3. Profiles of different winding functions: (a) primary and secondary fundamental parts, (b) secondary end effect parts.

$$\dot{B}_{re}=\frac{\dfrac{3\mu_0}{4g_e}N_sI_s(\dfrac{1}{\alpha_2}+sG\dfrac{\pi}{\tau}+j\dfrac{\pi}{\tau_e})}{(\dfrac{1}{\alpha_1}+\dfrac{1}{\alpha_2}+j\dfrac{2\pi}{\tau_e})(1+jsG)}\exp(-x/\alpha_1)\exp[j(\omega_e t-\frac{\pi x}{\tau_e})] \quad (11)$$

From [5], $\dot{I}_{re}$ is

$$\dot{I}_{re}=K\frac{1}{1+jsG}I_s\exp(j\omega_e t) \quad (12)$$

where K is a function of the SLIM velocity and primary length, etc. From (10) to (12), the secondary end effect winding function $\dot{N}_{re}$ is shown as

$$\begin{cases} N_{\alpha re}(x)=-\dfrac{N_2}{K}\exp(-x/\alpha_2)\sin(\pi x/\tau_e-\theta_e) \\ N_{\beta re}(x)=\dfrac{N_2}{K}\exp(-x/\alpha_2)\cos(\pi x/\tau_e-\theta_e) \end{cases} \quad (13)$$

where N_2 and θ_e are related with the slip, goodness factor and SLIM structural parameters.

According to aforementioned three groups of winding function equations, their profiles are indicated in Fig. 3 based on a 6-pole SLIM. It is interesting to see that the primary two-axis parts are the same as the secondary fundamental ones, which are sinusoidal waves within the primary length. For the influence of primary half-filled slots, the β-axis wave can be regarded as lagging the α-axis one by $\pi/2$. The secondary end effect parts attenuate gradually from entrance side to exit side for the longitudinal end effect influence.

The SLIM voltage equation in matrix form is given by

$$\vec{u} = [R]\vec{i} + \frac{d\vec{\lambda}}{dt} + v_2 \frac{\pi}{\tau}[U]\vec{\lambda} \tag{14}$$

where several vectors are expressed by the following.

$$\vec{\lambda} = [L]\,\vec{i}\ ,\ \vec{u} = [u_{\alpha s}, u_{\beta s}, 0, 0]^T\ ,\ \vec{i} = [i_{\alpha s}, i_{\beta s}, i_{\alpha r}, i_{\beta r}]^T\ ,$$

$$[R] = \begin{bmatrix} R_s & 0 & 0 & 0 \\ 0 & R_s & 0 & 0 \\ 0 & 0 & R_r & 0 \\ 0 & 0 & 0 & R_r \end{bmatrix},\ [U] = \begin{bmatrix} 0 & 0 & 0 & 0 \\ 0 & 0 & 0 & 0 \\ 0 & 0 & 0 & 1 \\ 0 & 0 & -1 & 0 \end{bmatrix}.$$

where L is an inductance matrix, in which the element between any two winding functions mentioned in (5), (9), (13) may be calculated by

$$L_{12} = \frac{2\mu_0 l_\delta}{3g_e} \int_0^{p\tau} N_1(x) N_2(x) dx \tag{15}$$

where N_1(x) and N_2(x) are two arbitrary winding functions, l_δ is the primary stack width, and p is number of primary poles. There are 36 inductances to be calculated, where 18 of them are independent [5].

According to the energy conversion balance theorem between primary and secondary, the thrust is

$$F_e = (3\pi/2\tau)[i_1]^T [G][i_1] \tag{16}$$

where matrix i_1 including the end effect part is expressed by

$$[i_1] = [i_{\alpha s}, i_{\beta s}, i_{\alpha r}, i_{\beta r}, (i_{\alpha s} + i_{\alpha r}), (i_{\beta s} + i_{\beta r})]^T \tag{17}$$

and matrix G is the speed voltage coefficient matrix, which may be calculated in the similar way of inductance matrix L.

The input active power is

$$p_{in} = \frac{3}{2}(u_{\alpha s} i_{\alpha s} + u_{\beta s} i_{\beta s}) \tag{18}$$

The input reactive power is

$$q_{in} = \frac{3}{2}(u_{\beta s} i_{\alpha s} - u_{\alpha s} i_{\beta s}) \tag{19}$$

The output active power is

$$p_{out} = (F_e - F_m) v_2 \tag{20}$$

where F_m is the total mechanical resistant force involving wind and friction forces.

The power factor is

$$\cos\varphi = p_{in} \Big/ \sqrt{{p_{in}}^2 + {q_{in}}^2} \tag{21}$$

The efficiency is

$$\eta = p_{out} / p_{in} \tag{22}$$

III. Simulations and Experiments

The above derivations describe the dynamic state of SLIM in differential linkage equations. The equations could be solved by numerical method step by step. In most dynamic cases, the state variables include the secondary linkages and primary currents. The equations can also be readily used for steady-state analysis, which can be calculated by simply setting d/dt to jω_e in (14). The SLIM main dimensions are shown in table I.

TABLE I
Dimensions of the SLIM

Pole pitch	Pole pairs	Primary length/width
0.2808 (m)	4	2.476/0.3 (m)
Secondary width	Secondary sheet thinkness	Air gap
0.36 (m)	7 mm, Copper	9 (mm)
Base frequency	Thrust	Primary phase voltage
25 (Hz)	25 (kN)	635 (V)
Line current	Number of slots	Secondary sheet width
280 (A)	79	0.36 (m)

Fig. 4 shows the constant current start-up process, including the velocity, thrust, secondary fundamental-, and eddy-current curves. In the overall operation region, the motor has constant stator current of 280 A and constant primary frequency of 10 Hz. The secondary fundamental current, similar to that of RIM, decreases gradually as the speed rises, and equals zero at the synchronous point. However, the secondary end effect part ascends with its incremental speed, and reaches the maximum at the synchronous speed for the quick air gap flux linkage change resulted from the longitudinal end effect.

Fig. 5 shows the variable frequency variable voltage start-up process. The primary frequency varies from 2 to 25 Hz with proportionally increasing primary voltage so as to keep a comparatively constant air gap flux linkage. The testing task was carried out on one linear metro line cooperated with a Chinese company. The primary two-phase voltages, two-phase currents, and operating speed are sampled by corresponding sensors, and input to a Yokogawa DL750 oscillometric recorder. The sampling frequency for voltage is about 20 kHz, which can be input directly into the dynamic equations to achieve SLIM primary phase current and velocity step by step. The simulation results of stator phase current and velocity are given in Fig. 5, where comparisons have been made with the measurements. It can be seen that the calculations agree with the measurements approximately.

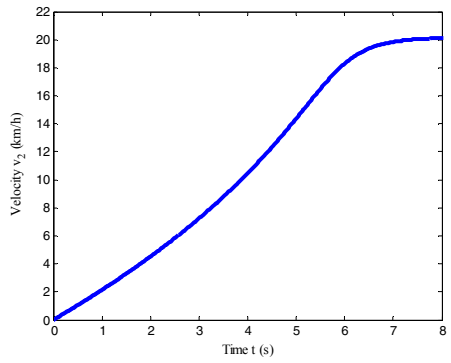

(a)

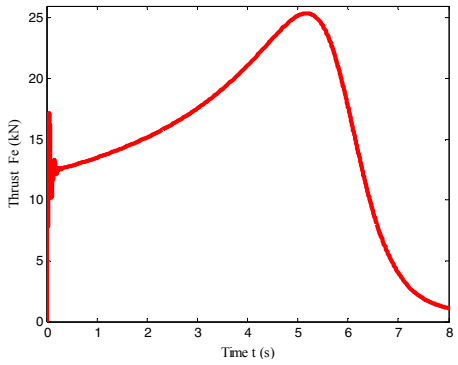

(b)

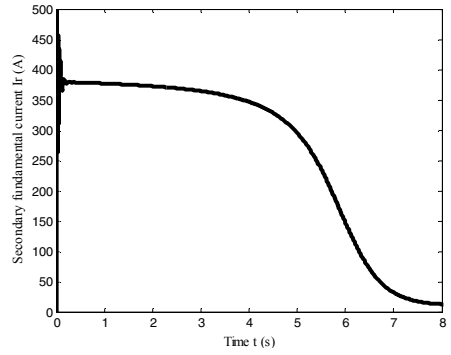

(c)

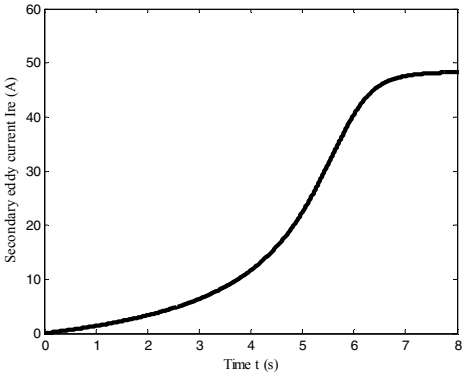

(d)

Figure 4. Constant current start-up performance analysis: (a) velocity, (b) thrust, (c) secondary fundamental current (RMS), and (d) secondary eddy current (RMS).

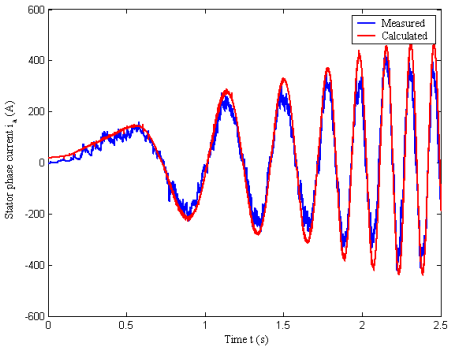

(a)

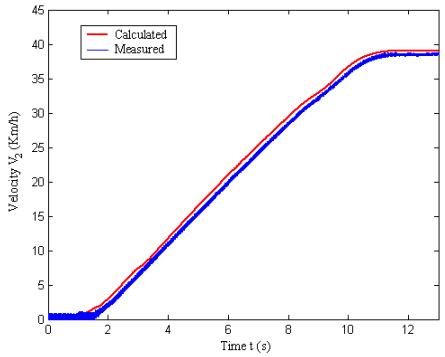

(b)

Figure 5. Variable frequency variable voltage start-up performance analysis: (a) stator current, (b) velocity.

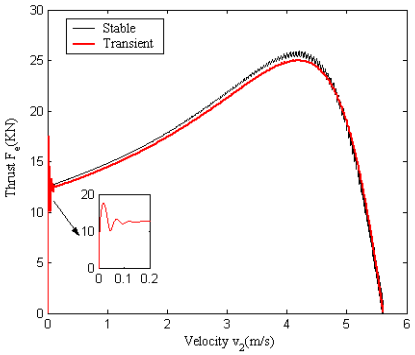

Figure 6. Thrust curves with constant current constant frequency calculated at steady-state and dynamic states.

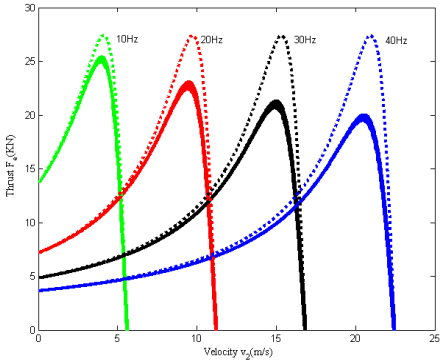

Figure 7. Thrust curves with constant current variable frequency calculated at steady state.

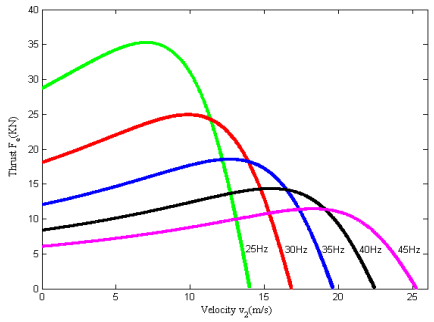

Figure 8. Thrust curves with constant voltage variable frequency calculated at steady state.

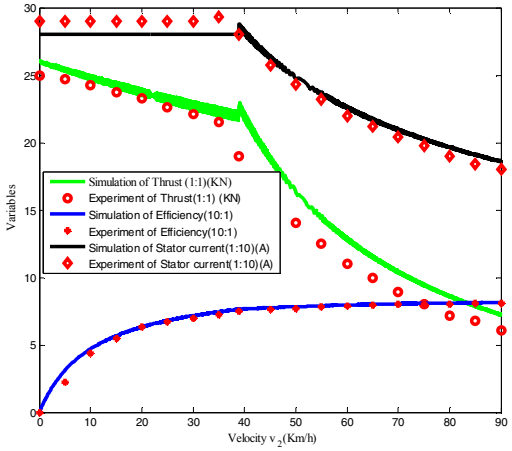

Figure 9. Simulated and measured performance curves.

Fig. 6 shows the thrust curves calculated by the steady and dynamic states equations. In the whole range, the primary current is controlled to be constant, 280 A, and the primary frequency is also a constant, 10 Hz. It is apparent that the steady-state thrust is very close to the dynamic one. It is interesting to observe that there are double frequency (20 Hz) thrust ripples as SLIM starts up. This is due to the electromagnetic dynamics in the secondary circuits produced by the longitudinal end effects [5].

Fig. 7 plots the thrust curves calculated by steady state equations when the primary current is kept constant, 280 A. Dash lines indicate the thrusts without end effects, while continuous lines are with end effects. Due to the longitudinal end effect, the maximal thrust will decrease as the velocity goes up [3]-[5].

Fig. 8 shows the thrust curves calculated by steady state equations when the primary phase voltage is kept constant, 635 V. The trend of thrust is similar to that in Fig. 7. For greater current reduction by increasing frequency at constant voltage, the maximal thrust decreases more quickly than that at constant current.

The thrust of SLIM in transportation is one of the most important factors. The actual SLIM control scheme often includes two regions, i.e. "constant current" and "constant power" regions. Below the base speed, the primary phase current and slip frequency are kept constant. Due to the power conditioner voltage limitation, constant voltage operation is encountered above the base speed. The phase current decreases very quickly due to the increasing total impedance. In order to meet the drive system requirement, it is necessary to increase the slip frequency linearly to prevent quick thrust reduction.

This paper has analyzed the SLIM steady-state drive performance in the overall working region and compared simulations with measurements including the phase current, thrust and efficiency curves as shown in Fig. 9. The base speed is 40 km/h. Simulation evaluations on the phase current, thrust, and efficiency are made according to the steady equations of the winding function equations. The experimental setup and measurement values are referred in [4]. Simulated phase current is close to its measurement, which is kept constant below base speed and decreases linearly beyond that. The thrust below the base speed decreases a little as the speed goes up for the end effect although the phase current is constant. Beyond the base point, thrust decreases linearly for the reducing phase current. Error in the base speed is obvious because the control manner and slip frequency have been changed. The efficiency calculation and measurement agree with each other, which meet engineering application requirement.

IV. CONCLUSIONS

This paper has presented a new equivalent model of SLIM based on winding function method. It supposes the SLIM has three groups of winding functions, i.e. primary, secondary fundamental, and secondary end effect ones. The primary stationary two-axis winding functions have been derived from the stationary three-phase winding distributions jointed by 3/2 static-axis transformation. The secondary fundamental and end effect ones have been gained based on the electromagnetic relationship between primary and secondary. According to the three groups of winding functions, the influence by longitudinal end effect and half-filled slots can be automatically described by corresponding end effect mutual inductances and half-filled slot inductances. Moreover, the equivalent voltage and linkage equations have been deduced to analyze both steady and dynamic performances in a similar way as that of RIM. By comprehensive simulation and/or experiments on different working states, the proposed model can be regarded as a useful tool to investigate different SLIM dynamic performances, steady-state performances, and control schemes.

REFERENCES

[1] Xialing Long, *Theory and magnetic design method of linear induction motor*, China: Science Publishing Company, 2006.

[2] G. Kang and K. Nam, "Field-oriented control scheme for linear induction motor with the end effect," *IEE Proceeding on Electrical Power Application*, vol. 152, no. 6, pp. 1565-1572, Nov. 2005.

[3] J. Duncan, "Linear induction motor equivalent circuit model," *IEE Proc.*, vol. 130, part B, no.1, pp.51-57, Jan.1983.

[4] Tsuyoshi Higuchi, Sakutaro Nonaka, "On the design of high efficiency linear induction motors for linear metro," *Electrical Engineering in Japan*, vol. 137, no. 2, pp. 36-43, Aug. 2001.

[5] Wei Xu, "Research on the performance of single-sided linear induction motor," *Doctoral Thesis of Chinese Academy of Sciences*, China, 2008.